Digital Shearography for NDT: Determination and Demonstration of the Size and the Depth of the Smallest Detectable Defect

Bicheng Guo, Xiaowan Zheng, Marco Gerini-Romagnoli, Lianxiang Yang*

Abstract

This paper presents a methodology of digital shearography for determining the size of the smallest detectable defect and the depth under different loading magnitudes for the purpose of nondestructive testing. Digital Shearography, an interferometric nondestructive testing (NDT) technique, has been proven to be a useful tool for material inspections and evaluations, especially for detecting delaminations/disbonds in composite materials and honeycomb structures. A commonly asked question in the field of NDT is about measuring sensitivity - specifically, what is the smallest detectable delamination/disbond and how deep can these be detected? Although various attempts to find the smallest detectable defect by shearography have been made, a numerical model for determining the size of the smallest detectable defect and the depth has not yet been developed. This paper did a study in this aspect, especially for NDT of delamination and disbond in polymers and honeycomb structures. First, a mechanical model based on the thin plate theory to calculate the expected bending of close-to-surface defects was proposed; the model built a relationship among the deformation caused by a defect, the size and the depth of the defect, as well as the load and the material properties. Second, the relationship between the relative deformation measured by shearography and the deformation induced by a defect was established based on the optimized shearing amount and the sensitivity of digital shearography. Based on these analyses, relationships between the size of the smallest detectable defect and the depth under different load amounts were established for different defect shapes. Finally, experimental validation based on different sizes of prefabricated defects were conducted to verify these relationships. The experimental results show that the model developed can provide useful estimation for NDT by digital shearography, especially with helping test engineers estimate the size of the smallest detectable defect and the depth with corresponding loading magnitudes.

Keywords: Digital shearography, NDT, the smallest detectable size, effect of defect depth, effect of defect shape, impact of loading magnitude

1. Introduction

Honeycomb core sandwich composites and composites like glass/carbon fiber reinforced plastic (GFRP and CFRP) have superior strength-to-weight ratios, high resistance to corrosion and fatigue, and are widely used in aerospace and automotive industry. Unfortunately, these kinds of materials easily produce disbonds between the inner core and outer skin for honeycomb structures and delaminations between the laminated layers for GFRP and CFRP due to impact loading, aging, imperfect manufacturing, etc. Different NDT methods have already been applied to test for such kinds of defects [1-3]. However, optical methods such as thermography, holography, electronic

speckle pattern interferometry (ESPI), and shearography are emerging as strong candidates for new industrial NDT tools because of their whole field, non-contacting, and non-contaminating properties [4-9]. Among these optical methods, the shearographic method seems more efficient and practical for NDT testing [10-15]. Shearography is a coherent-optical method that is similar to Holography and ESPI, but displays many advantages for industrial applications due to its direct measurement of strain information: (1) A rigid body movement generates a displacement, but no strain, thus, shearography is relatively insensitive to environment interruptions and it is more practical for industrial application; (2) defects in objects usually induce strain concentrations, thus, it is easier to reveal defects with strain anomalies than with displacement anomalies; (3) shearography uses a self-reference interferometric system which has low requirement for laser coherent length and enables the use of economical and practical diode laser or multi diode lasers if a larger area is inspected. These substantial advantages have led to shearography being one of the best NDT tools for composite materials, especially for honeycomb structures [16-18].

Digital shearography, also called electronic shearography or TV shearography, uses a digital camera as the recording device combined with different measurement and evaluation algorithms to enable a real time measurement and quantitative evaluation of shearogram [19-20]. In the past two decades, digital shearography has been widely used in the field of NDT of composite materials [21-25]. The main application is to detect disbonds in honeycomb structures and delaminations in GFRP and CFRP composite materials [26-28]. Although there exist many advantages of digital shearography, a successful shearographic inspection depends on highlighting the contribution of defect-induced surface deformation and the smallest measurable deformation of the shearographic system. The defect-induced deformation is a complex parameter which is related to loading magnitude, loading method, shearing amount, defect size, depth, shape, and so on [29]. In the past two decades, quite a number of researchers conducted studies on shearographic NDT for different sizes and/or depths under different loading methods. E.C. Krutul, R.M. Groves et al. reported in 2011 a modelling of opto-mechanical measurement system, including shearography instrument, loading technique and the response of the object under test and the comparison of the simulation results with experimental results. This approach is suitable to understand the response of components under load and to predict anomalies such as defects [30]. In the next year (2012), G. De Angelis et al. reported a new numerical-experimental model to detect size and depth of flat bottom holes in metallic and laminated composite structures by digital shearography based on dynamic response of defects to applied stresses [31]. Another numerical-experimental model to test defected materials by digital shearography based on thermal loading was reported by D. Akbari et al. in 2013 [32]. Hybrid methods based on experimental and computational investigations using shearographic test results and finite element analysis software and/or Matlab to predict internal defects were reported by X. Chen et al. (2015), Y. Fu et al. (2017) and J.F. Vandenrijt et. al. (2019), respectively [33-35]. Although these studies have provided useful information in the area of shearographic NDT, a systematic study to show the relationships between the size of the smallest detectable defects and the depths under different loading magnitudes for NDT by the shearographic testing method has not yet been conducted.

In this paper, we developed a mechanical model to quantitatively present the relationships between the size of the smallest detectable defects and the depths under different loading magnitudes for NDT by the shearographic testing method. A mechanical model based on the elastic mechanics and the plate theory was first built. The differential equation of the deformation and the solutions of the deformation were then presented for different defect shapes at given boundary conditions. Although thermal loading is the easiest loading method, vacuuming or and some internal pressure is more effective loading method because such kind of loading will tear apart disbonds and delaminations which cause the surface deformation larger and make NDT of the defects easier. Using this loading method, numerical equations for determining the size of the smallest detectable defect and the depth based on the smallest measurable deformation or the relative deformation of digital shearography were developed. Experimental validation was conducted and the results agreed with the numerical equations.

2. A Brief Review of Digital Shearography

2.1 Principle of shearography

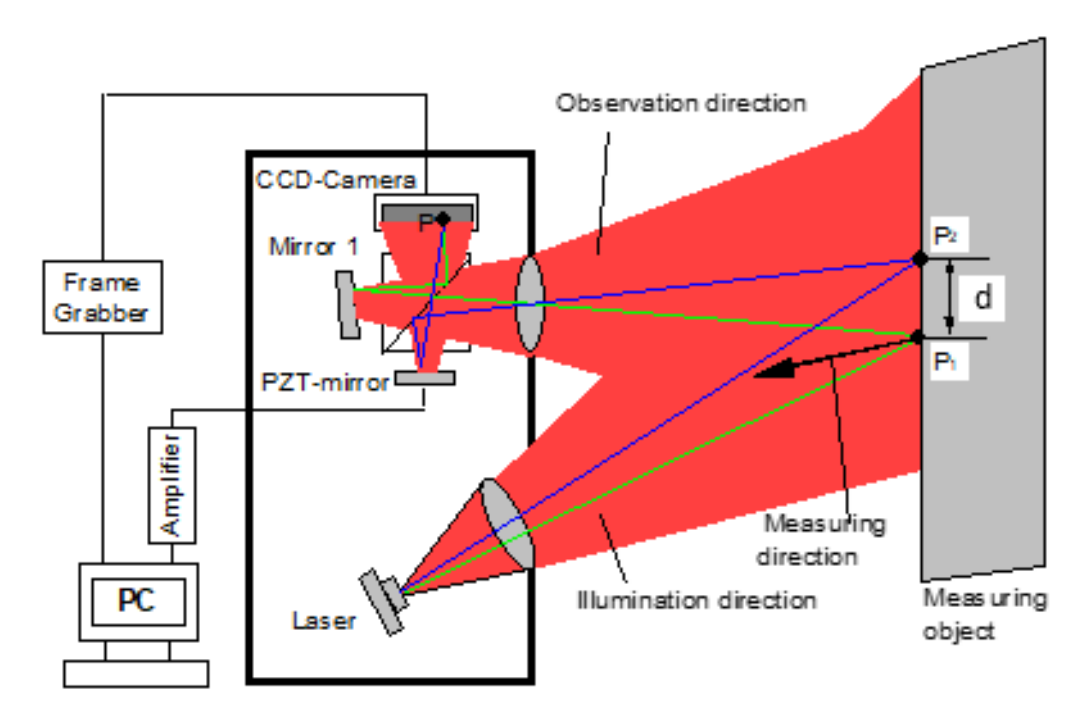


Fig. 1. Principle of digital Shearography

Fig. 1 shows the typical shearographic setup in which a modified Michelson interferometer is used as a shearing device. By tilting mirror 1 by a very small angle, the system can cause two non-parallel rays of light scattered from two different object points to interfere with each other. The distance and the orientation between these two points are called the shearing amount and the shearing direction, respectively. As the object surface is diffusely reflective, the interference of the scattered rays yields a random pattern known as speckle pattern. When the object is slightly deformed, the speckle pattern will be slightly changed. A visible fringe pattern, called shearogram, can be observed by conducting a digital subtraction of the intensities of the two speckle patterns, which will be explained in detail below.

2.2 Formation of shearogram

The intensity "I" of the speckle pattern before loading can be expressed by [36]:

$$I = A + B \cos \phi \tag{1}$$

where A is the background, B is the modulated term which is related to the image contrast γ ($\gamma = B/A$), and ϕ is the phase difference between two points with the shearing distance in the shearing direction. Fig. 2a shows the intensity image of the speckle pattern before loading.

After the object is loaded, the phase difference between the two points becomes $\phi' = \phi + \Delta \phi$, where $\Delta \phi$ is the relative phase change, resulting from a relative deformation between P₁ and P₂. The intensity of the speckle pattern after loading then becomes the follows:

$$I' = A + B\cos\phi' = A + B\cos(\phi + \Delta\phi) \tag{2}$$

Fig. 2b shows the intensity image of the speckle pattern after loading. A fringe pattern, or shearogram, which is shown in Fig. 2c, can be obtained by a direct subtraction between the intensity images of the speckle patterns before and after loading. Because the intensity value must be positive, the absolute value will be displayed, represented as follows:

$$I_{s} = |I' - I| = B |\cos(\phi + \Delta\phi) - \cos(\phi)|$$
(3)

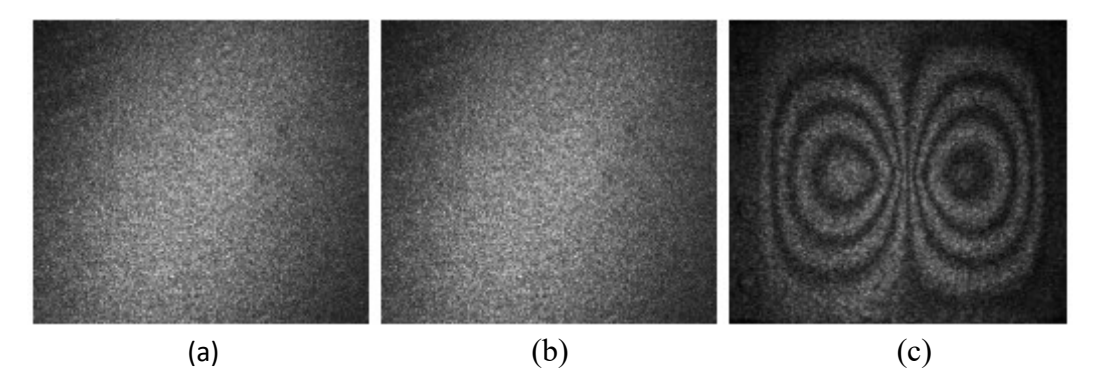


Fig. 2. Intensity images of the speckle pattern before loading (a), after loading (b), and the shearogram obtained by a digital subtraction between these two intensity images (c)

Dark fringes appear on the shearogram when $I_s = 0$, i.e. $\Delta = 2n\pi$ (n = 1, 2, 3...). The shearogram is therefore displayed as a highly visible fringe pattern. Due to the relative phase difference between two adjacent fringes being equal to 2π , the phase at each fringe can be determined by counting the shearogram fringes. Then the relative deformation can be determined based on the relationship between the relative phase change and the relative deformation between points P_1 and P_2 .

For digital shearography NDT, the angle between the illumination direction of the laser and the observation direction of the digital camera is usually small or close to zero, Under this condition, the relative deformation Δw between the two points with the shearing amount in the out-of-plane direction is given by [37]:

$$\Delta w = (\lambda/4\pi)\,\Delta\phi\tag{4}$$

where λ is the wavelength of the laser used.

Eq. (4) shows that the relative deformation Δw is proportional to the relative phase difference $\Delta \phi$. Thus, the measuring sensitivity for the relative deformation depends on the smallest measurable $\Delta \phi$. In the shearographic interferometry, the relative phase difference $\Delta \phi$ can be determined by the intensity subtraction method as shown in Fig. 2 and the phase shift method. In the intensity subtraction method, the smallest measurable value of the relative phase difference $\Delta \phi$ is 2π because the smallest integer number is 1. Therefore, the smallest measurable Δw is $\lambda/2$ based on Eq. (4). In the phase shift method, phase values less than 2π can be measured. According to the methods to produce phase shifts, they can be divided into two categories: temporal phase shift digital shearography (TPS-DS) and spatial phase shift digital shearography (SPS-DS). The temporal phase shift method needs to record multiple frames and introduce phase shift between each frame in time series. It is highly accurate and is usually used for static measurements (also for dynamic if vibration is harmonic) [38], while the spatial phase shift method introduces the phase shift in space series and requires only a single frame for phase determination [39-40] which is well suited for dynamic measurements. Usually, the spatial phase shift method has a relatively complicated optical setup and a small aperture requirement which demands higher laser power. With the continuous improvement in technology in recent years, the spatial phase shift method has begun to be used in the commercial digital shearographic system [39-42], however, the temporal phase shift technique is still by far the most popular method used in the commercial digital shearography system due to its simple optical setup and easy implementation. All phase maps in the following sections were obtained by the temporal phase shift method.

Compared to the intensity subtraction method in which the smallest measurable phase is 2π , the phase shift method has much higher phase measurement sensitivity. Considering speckle noise, smooth algorithm, and other factors, the measurement sensitivity of phase shift method-based digital shearography can reach between $2\pi/5$ and $2\pi/10$, which is about 5 to 10 times higher phase measuring sensitivity than the intensity subtraction method, depending on the test environment, hardware setup, and software algorithm. According to Eq. (4), the measuring sensitivity of relative deformation $\Delta w \left[\Delta w = (\lambda/4\pi) \Delta\phi\right]$ can reach between $\lambda/10$ and $\lambda/20$. The application of phase shift methods has led to tremendous enhancement of the measuring sensitivity in digital shearography. Therefore, smaller defects can be found. A comparison of shearographic tests using intensity subtraction and phase shift methods are shown in Fig. 3.



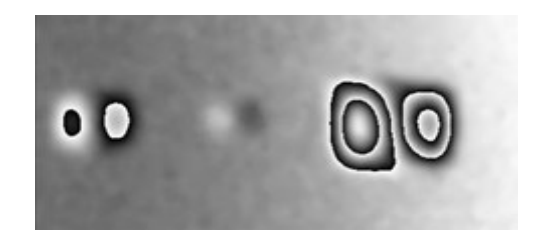


Fig. 3. Comparison between the intensity subtraction version (left) and the phase-shift method (right), a smaller defect in the middle become visible in the phase shift shearography

3. Digital Shearography for Non-Destructive Testing (NDT)

3.1. Principle of shearography for NDT

The fundamentals of shearography for NDT is to find internal defects/delaminations by measuring the surface anomalies from the distribution of Δw caused by a minor loading. Fig. 4 shows how the shearography works for NDT. When an object with an internal defect (Fig. 4a) is loaded, such as by a vacuum loading (Fig. 4b), the surface in the defect area will cause a relatively larger deformation (Fig. 4c) than other areas, and the maximal deformation occurs in the middle of the defect area. Shearography measures a relative deformation " Δw " between two points with a shearing amount (Fig. 4d). If the shearing amount selected is half or more than the size of the defect, the maximum relative deformation Δw measured by shearography is equal to the maximal deformation in the defect area, denoted as w_{max} as shown in Fig. 4d. Usually, the smallest sized defect which should be detected is known or is set by the user of the materials; therefore, an optimized shearing amount can be selected and the maximum measurable relative deformation is the maximum deformation w_{max} in the defect area.

Now, the question is what kind of defects can be found? If the deformation caused by a loading in the defect area is larger than the smallest measurable deformation w_{max} by the digital shearography, such kinds of defect should be detectable. According to the discussions in section 2.2, the smallest measurable deformation w_{max} is ranged from $\lambda/10$ and $\lambda/20$, depending on the test environment, the hardware setup, and software algorithm. The deformation caused by the loading is also related to the defect size S, the depth t from the surface, material properties, etc. (Fig. 5). In order to estimate the smallest detectable defect, the analysis of the relationship among these parameters is mandatory.

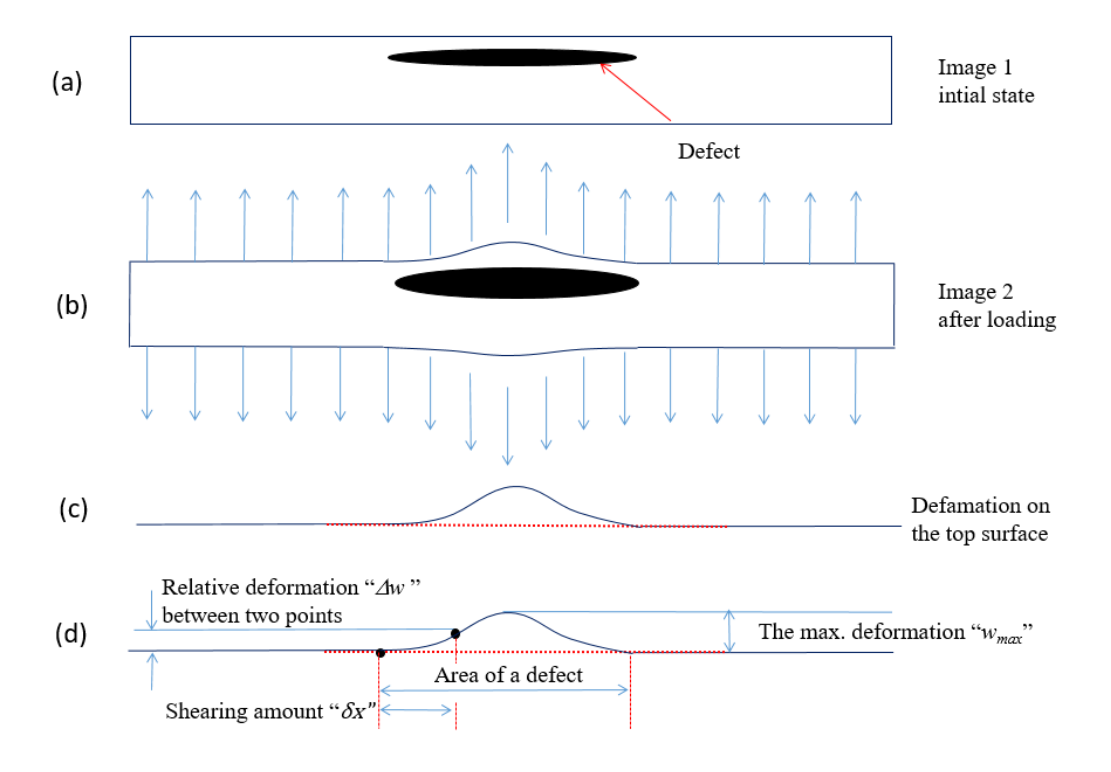


Fig. 4. Fundamentals of shearography for NDT: (a) an object with a defect, (b) deformation after a loading, (c) the shape of the deformation, and (d) relationship between the relative deformation and the shearing amount

3.2. Relationship among the deformation caused by loading, the size and depth of the smallest detectable defect

3.2.1. Mechanical model

In order to discuss the relationship between the deformation caused by loading in the defect area and the size and the depth of the smallest detectable defect, a numerical method to calculate the deformation should be studied first. Fig. 5 shows deformations of a disbond between a surface sheet and a honeycomb core in a honeycomb structure and a delamination in a CFRP or GFRP panel under a pulling force, such as a vacuum loading, respectively. It should be emphasized here that the study is based on the fact that the defect is not far from the object surface. The depth of the defect t should be less than $1/5 \sim 1/8$ of the defect size and the loading is perpendicular to the surface. With these assumptions, the top parts of the defects can be counted as plates. From a mechanical point of view, these deformations are equivalent to the deformation of the plate under a loading of internal pressure as shown in Fig. 6. If the size of the hole underneath the plate is t and t and t are the radius of a circular shape or the half side of a rectangular shape) and the thickness of the top plate is t, the deformation shown in Fig. 6 can approximately be considered as the model of deformation in the area of the disbond or the delamination shown in Fig. 5.

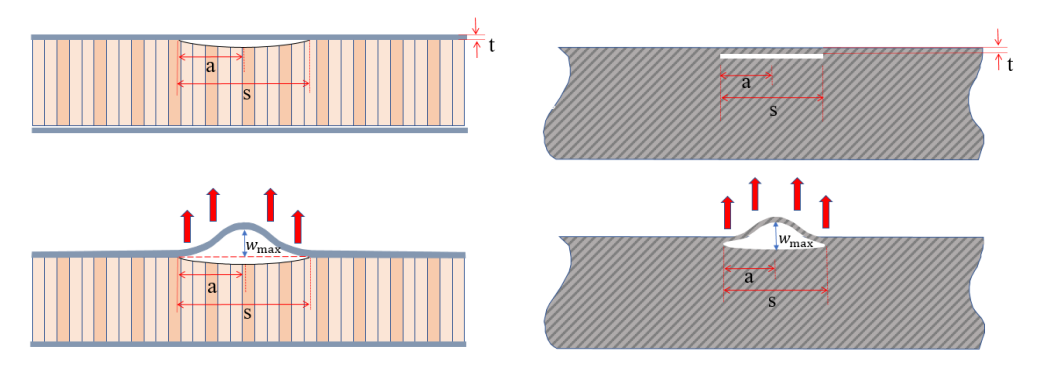


Fig. 5. Defects and the deformation under a pulling force: a disbond in a honeycomb structure (left), and a delamination in a CFRP/GFRP panel (right)

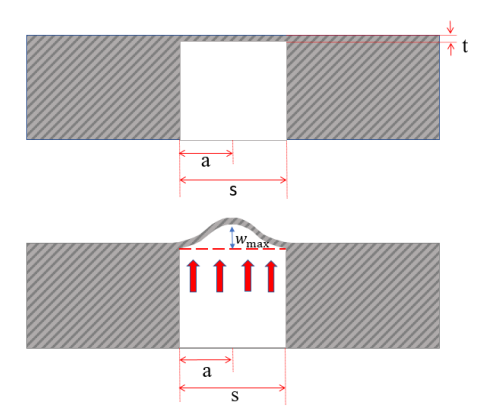


Fig. 6. An equivalent deformation for a plate with a hole underneath under an internal pressure.

If the loading is perpendicular to the surface and the thickness t is much smaller than the size of S [$t < (1/5 \sim 1/8) xS$], the upper part of the hole can approximately be regarded as a plate fastened all around under pure bending and twist. According to the elastic mechanics and the plate theory, the differential equations of the deformation for the plate shown in Fig. 6 is given by [43]:

$$\nabla^2 \nabla^2 w = \frac{\Delta p}{D} \tag{5}$$

where w is the out-of-plane deformation, Δp is the magnitude of internal pressure, D is the flexural rigidity, ∇^2 and D are shown as follows:

$$\nabla^2 = \frac{\partial^2 w}{\partial x^2} + \frac{\partial^2 w}{\partial y^2} \tag{6}$$

$$D = \frac{E t^3}{12 (1 - v^2)} \tag{7}$$

In Eq. (7), E is the elastic modulus of the material, ν is the Poisson ratio, and t is the thickness of the plate which is equivalent to the depth of defects. The solution of Eq. (5) depends on the shape of the defect, the method of loading and boundary conditions. In our study, we will discuss defects in two shapes, one is circular and the other is rectangular or square.

3.2.2. Deformations of defects with different shapes

Circular defect

First, we will discuss the deformation of a defect with a circular shape. Assuming that the circular defect has a radius of "a", its depth is t, and the origin of coordinates is in the middle of the defect, the loading and the boundary conditions are listed below:

- Loading method: internal pressure (a uniform load),
- Boundary conditions: Fastened all around, i.e. $w \mid_{x=a} = 0$, $\partial w / \partial x \mid_{x=a} = 0$,

Under these conditions, the solution of differential Eq. (7) for deformation w is given by [44]:

$$w = \frac{\Delta p}{64 D} \left[a^2 - (x^2 + y^2) \right]^2 \tag{8}$$

and the maximum deformation w_{max} occurs in the middle of the plate, i.e. at x = 0 and y = 0:

$$w_{max} \mid_{circular} = \frac{\Delta p}{64 D} a^4 \tag{9}$$

where Δp is the magnitude of the internal pressure, a is the radius of the defect which is half of the size of the defect S, i.e. S = 2a. Substituting Eq. (7) for the flexural rigidity D in Eq. (9), the maximum deformation w_{max} can be rewritten as follows:

$$w_{max}|_{circular} = 0.01172 \frac{(1-v^2)}{E} \frac{S^4 \Delta p}{t^3}$$
 (10)

Rectangular and square defect

If the defect is a rectangular shape with a size of 2ax2b (2a is the long side and 2b the short side). under the same loading method (i.e. an internal pressure) and boundary conditions (i.e. fastened all around) as the circular defect, the maximum deformation in the middle of the plate is given by [44]:

$$W_{max} \mid_{rectangular} = \frac{16 a^4 b^4}{\pi^4 \left[3(a^4 + b^4) + 2a^2 b^2 \right]} \frac{\Delta p}{D}$$
 (11)

If the ratio of the short side (2b) to the long side (2a) is denoted r (r = 2b/2a) and the defect size S is expressed as 2a, Eq. (11) can be simplified by substituting Eq. (7) for D:

$$w_{max}|_{rectangular} = 0.01543 \frac{8 r^4}{[3r^4 + 2r^2 + 3]} \frac{(1 - v^2)}{E} \frac{S^4 \Delta p}{t^3}$$
 (12)

For a square defect a = b, i.e. r = 1, Eq. (11) can further be simplified as:

$$w_{max}|_{square} = 0.01543 \frac{(1-v^2)}{E} \frac{S^4 \Delta p}{t^3}$$
 (13)

3.2.3. Relationship between smallest detectable defects and the depth under given loads

Eqs. (10 - 13) present the relationship of the maximum deformations in the middle of the defects with the material properties, the size and depth of defects, and the loading magnitude for defects with circular, rectangular, and square shapes, respectively. They can also be rewritten as an expression of depth of the defect t, in term of the defect size S(S = 2a), the loading Δp and the maximum deformation in the middle of the defects w_{max} :

$$t(S, \Delta p, w_{max}) \Big|_{circular} = 0.22714 \left[\frac{(1-v^2)}{E} \right]^{\frac{1}{3}} \left[\frac{S^4 \Delta p}{w_{max}} \right]^{\frac{1}{3}}$$
 (14)

$$t(S, \Delta p, w_{max}) \Big|_{rectangular} = 0.24896 \left[\frac{8 r^4}{[3r^4 + 2r^2 + 3]} \right]^{\frac{1}{3}} \left[\frac{(1 - v^2)}{E} \right]^{\frac{1}{3}} \left[\frac{S^4 \Delta p}{w_{max}} \right]^{\frac{1}{3}}$$
(15)

$$t(S, \Delta p, w_{max}) \Big|_{square} = 0.24896 \left[\frac{(1-v^2)}{E} \right]^{\frac{1}{3}} \left[\frac{S^4 \Delta p}{w_{max}} \right]^{\frac{1}{3}}$$
 (16)

If a defect under a certain loading causes a deformation and the maximum deformation w_{max} in the center of the defect shown in equations above reaches the smallest measurable deformation by shearography, then such a defect is detectable by shearography. Substituting the smallest measurable deformation value, i.e. the measuring sensitivity of deformation, into w_{max} in the equations, the corresponding values of S and t are the size of the smallest detectable defect and the depth. Therefore, the relationships between the size of the smallest detectable defect S and the depth t under a vacuum or a pressure loading can be determined by Eqs. (14 - 16) for defects with circular, rectangular, and square shapes, respectively.

What is the measuring sensitivity of deformation by digital shearography? As described in section 2.2 and 2.3, shearography measures a relation deformation Δw . In the intensity subtraction method, the measuring sensitivity of Δw is $\lambda/2$, whereas, it can reach 5 to 10 times higher if a phase shift technique is introduced, depending on different conditions such as the test environment, the optical setup, and the software algorithm. Although 10 times higher measuring sensitivity needs an optimized condition, it is relatively easy to reach 5 to 6 times higher measuring sensitivity, i.e. the measuring sensitivity of Δw reaches to $\lambda/10$ to $\lambda/12$.

According to the discussion in section 3.1, if the shearing amount is selected as a half size or bigger than half the size of a defect, the maximum relative deformation Δw measured by shearography is equal to the maximal deformation in the defect area as explained in Fig. 4d, i.e. the measuring sensitivity of digital shearography for a relative deformation is actually equal to the measuring sensitivity of w_{max} . In order to find the defect, the w_{max} caused by a loading should bigger than the measuring sensitivity of shearography, e.g. from $\lambda/10$ to $\lambda/12$.

Substituting the w_{max} with $\lambda/12$, the relationships between the size of the smallest detectable defect S and the depth t can be determined by Eqs. (14 – 16) for defects with circular, rectangular and square shapes, respectively. If an He-Ne laser is used in the setup, the value of $\lambda/12 \approx 53$ nm. Figs. 7 - 9 show these relationships under different loading magnitudes if the material is aluminum, i.e.

E = 70 GPa, v = 0.33. The data in the x- and y-axes in the figures represent the size of the smallest detectable defect and the depth, respectively. The right part below the curves stand for the sizes of defects which are bigger than smallest detectable defect, and thus the defects are detectable and considered visible. The left part above the curve stands for the sizes of defects which are smaller than smallest detectable defect, and thus the defects are not detectable, and considered invisible.

Using different material properties (i.e. the Young's Module "E" and the passion ratio " ν "), the curves for different materials, such as for GFRP or CFRP panels, can be created based on equations (14), (15) and (16).

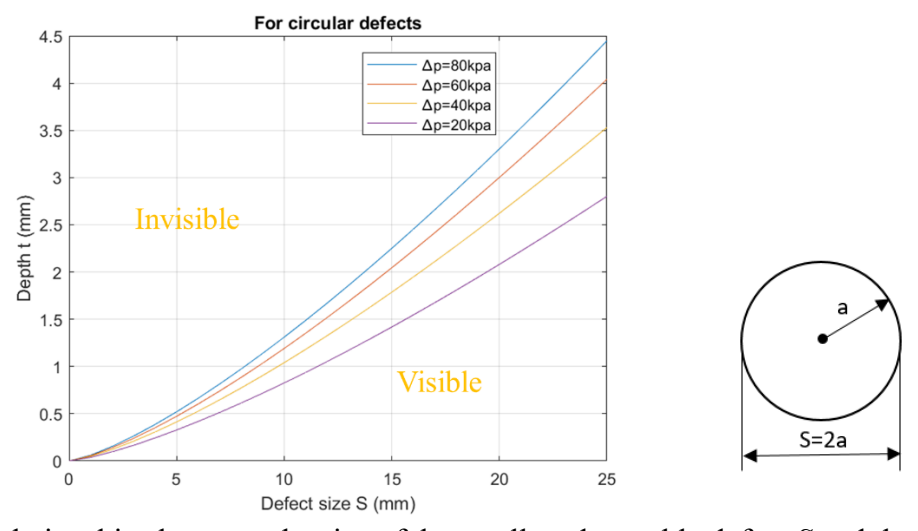
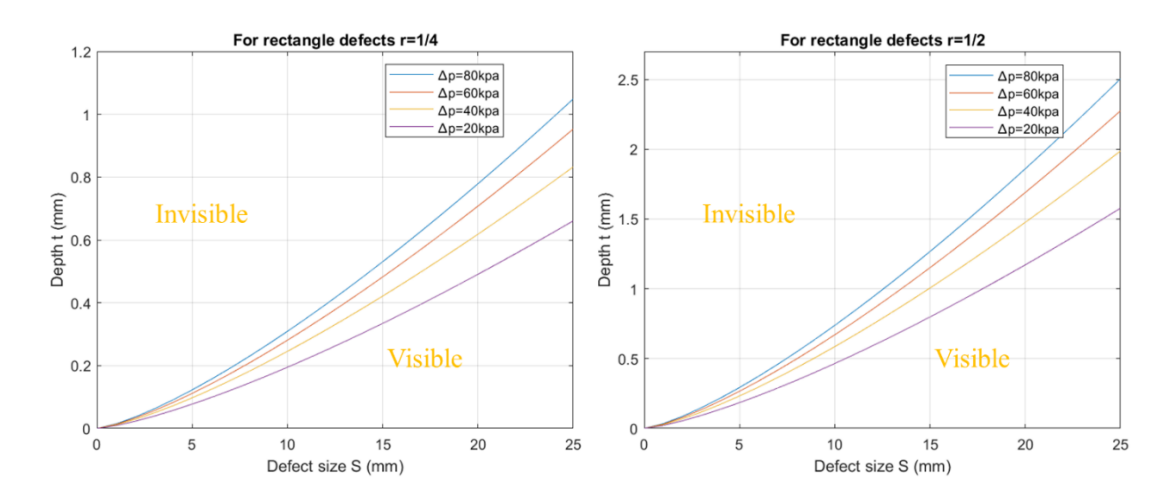
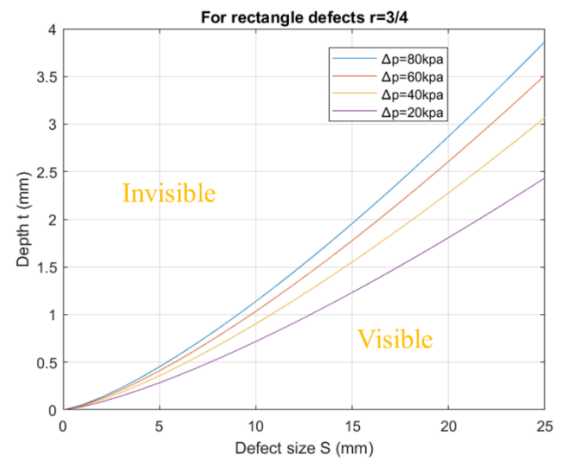


Fig. 7. Relationships between the size of the smallest detectable defect S and the depth t with a *circular* defect shape under different pressures (E=70 GPa, v=0.33 and w_{max} =53 nm)





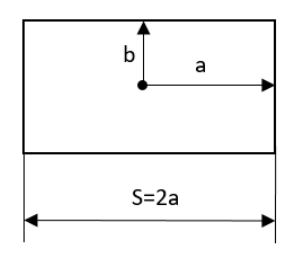
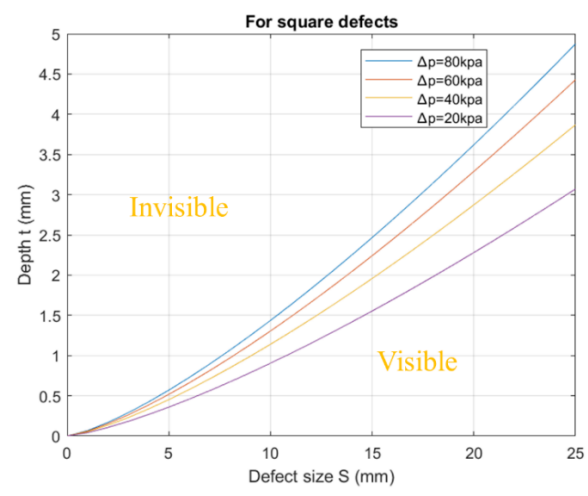


Fig. 8. Relationships between the size of the smallest detectable defect S and the depth t with a rectangular defect shape at different r values (r = b/a, E=70 GPa, v=0.33 and $w_{\text{max}}=53$ nm)



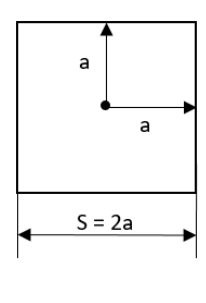


Fig. 9. Relationships between the size of the smallest detectable defect S and the depth t with a **square** defect shape under different pressure (E = 70 GPa, v = 0.33 and $w_{\text{max}} = 53$ nm)

4. Experiments

4.1 Specimen preparation

According to Eq. (14), defects were simulated by flat bottomed holes with different depths and sizes in aluminum plates with a total thickness of 12.7 mm (0.5 in) and a diameter of 166 mm. Five cylindrical holes were made 12.2 mm deep for one specimen with the diameter sizes ranging from 3, 4, 5, 5.9 and 8.2 mm, and 11.7 mm deep for the other specimen with the diameter sizes ranging from 5, 5.9, 8.2, 9.9 and 12 mm, respectively. With this design, the depth of the five simulated defects is t = 0.5 mm for the first specimen and t = 1 mm for the second specimen with boundary conditions of all around fixed.

Fig. 10 shows one of the samples with t = 1 mm. The 6 penetrating holes equidistantly distributed on the outer ring are used for fixing. The other 5 blind holes inside are used to simulate 5 defects of different sizes.



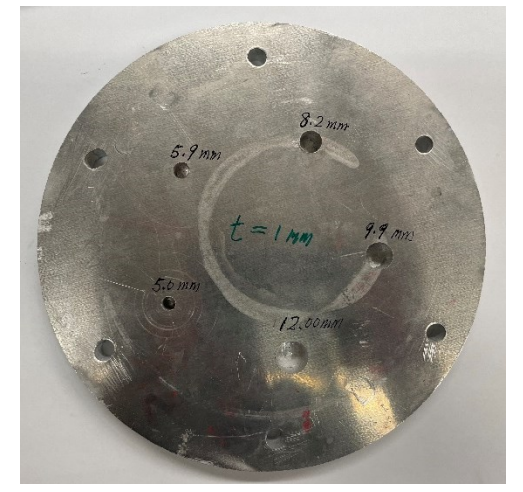




Fig. 10. The specimen of t = 1 mm with 5 simulated defects made by 5 flat bottomed blind holes of different diameters, left: back side, right: front side to be tested

4.2 Experimental setup and results

Fig. 11 shows the experiment setup. The aluminum plate was fixed in a cylindrical chamber which was connected to pressure pipe to generate a pressure load. The front surface of the aluminum plate was illuminated by an expanded He-Ne laser (50 mW) with a wavelength of 632.8 nm and tested by digital shearography with the phase shift technique. The camera has one mega pixel numbers and the shearing device is a modified Michelson Interferometer in which a Piezoelectric Transducer (PZT) driven mirror is used for the phase shift method. The shearing is in the x-direction, however, the shearing direction doesn't affect the results of the test if the defect is circular, square, or rectangular in shape, as discussed in this paper. The shearing direction will affect the test result when the defect is a narrow and long (much bigger than shearing amount) slot. Regarding shearographic tests of narrow and long slots, please refer to literature [45]. The shearing amount is 6 mm which is bigger than half of the diameter of each hole of the two specimens. Due to manufacturing limitations in our facilities, only cylindrical flat bottomed holes were made, i.e. only the defects with circular shape were experimentally tested.

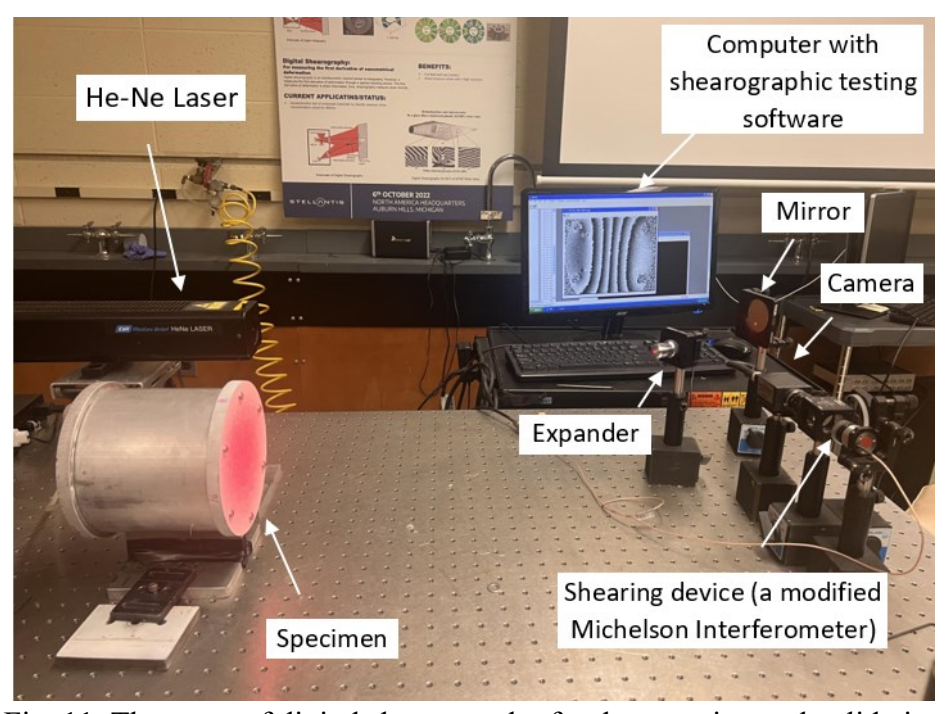


Fig. 11. The setup of digital shearography for the experimental validation

39 40

41

42

43

44

45

46

47

48

49

50

51

52

53

54

55

56

57

58

59

60

61 62

63

Fig. 12 shows the shearographic test results for the aluminum plate with five prefabricated defects whose depth t = 1 mm and whose size (diameter) ranges from S = 5, 5.9, 8.2, 9.9 and 12 mm, respectively. When the internal pressure reaches $\Delta p = 80$ kPa, three of the 5 defects can be found with the S = 8.2, 9.9, and 12 mm defects, respectively, marked in red circles. Please note that the noisy areas in the outer ring are the locations of fastening studs shown in Fig. 10 and are not defects. To clearly demonstrate the results with a better spatial resolution, the measurements were zoomed to each defect area (about 65 mm x 50 mm) to increase the pixel number between two adjacent fringes. By using one-megapixel camera, the display in the small area enhances the spatial resolution from the previous about 7 pixels/mm to about 15 pixels/mm. High spatial resolution means more pixel numbers between two adjacent fringes and more pixels lead to more grayscale points/values between two adjacent fringes. Therefore, the fringe pattern, the butterfly fringe pattern of shearography, becomes clearer. A comparison between the simulated curve of the smallest detectable defect size at t = 1 mm and the shearograms measured in each defect area of the aluminum plate at $\Delta p = 80$ kPa is shown in Fig. 13. As indicated above, the aluminum plate has 5 simulated defects whose size (diameter) ranges from S = 5, 5.9, 8.2, 9.9 and 12 mm, which correspond to the five shearograms in each defect area (from left to right), respectively. The experimental results agree with the numerical curve at t = 1.0 mm. According to the numerical curve, only defects larger than 8 mm can be detected at the given thickness and loading, and the experimental results have proved this as well. The shearograms in the areas with defect size of 5.0 mm and 5.9 mm don't show a butterfly pattern, so these two defects can't be detected (see the left two shearograms), whereas, the right three shearograms shows a clear butterfly pattern indicating that the defects of size 8.2, 9.9, and 12 mm can be detected.

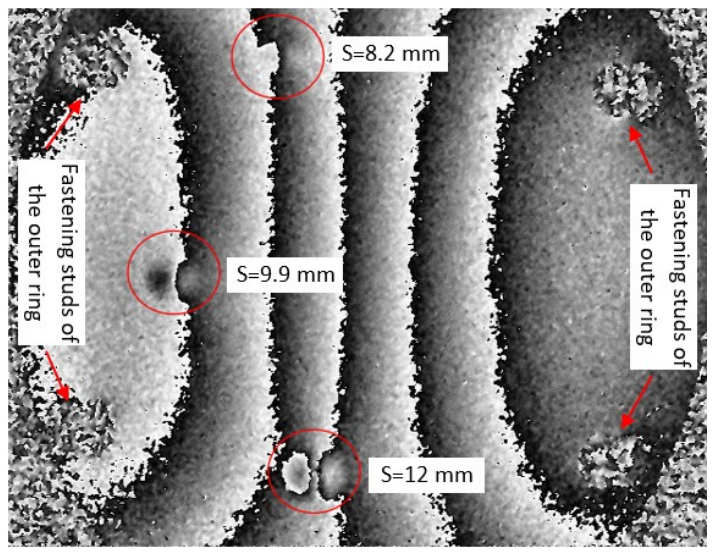


Fig. 12. Shearographic test results for the aluminum plate with five prefabricated defects whose thickness is t = 1 mm, and three of which were founded at $\Delta p = 80$ kPa

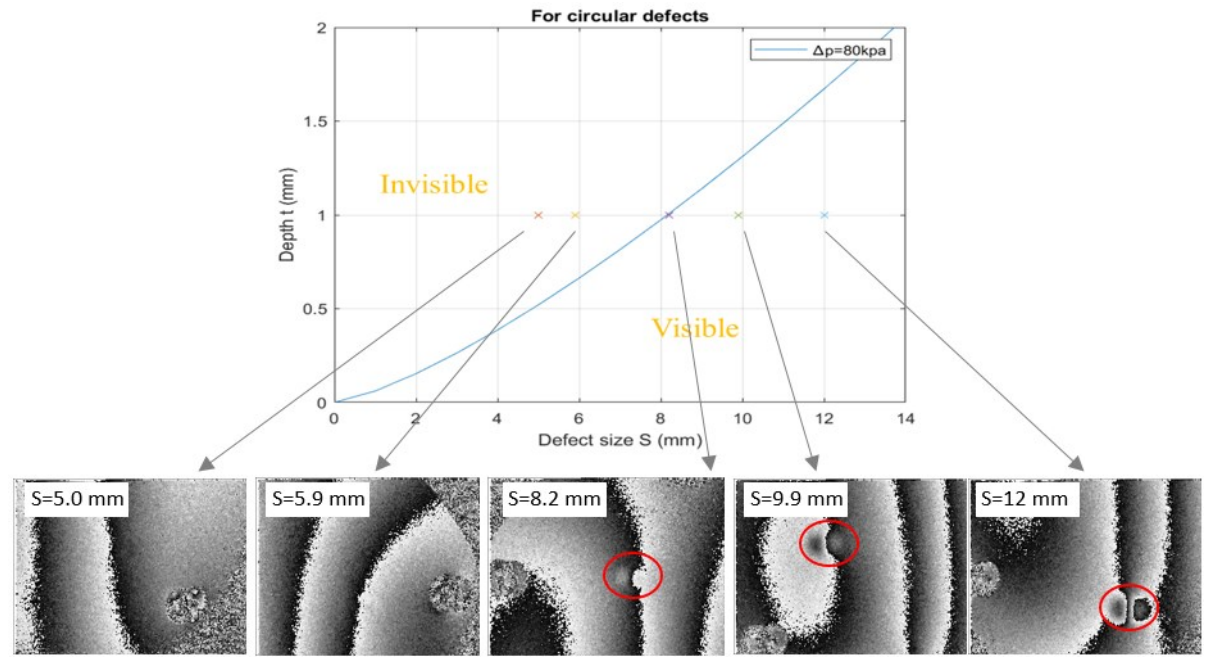


Fig. 13. A comparison between the simulated curve and the shearograms measured in the area of each defect of the aluminum plate with five prefabricated defects at t = 1 mm and $\Delta p = 80$ kPa.

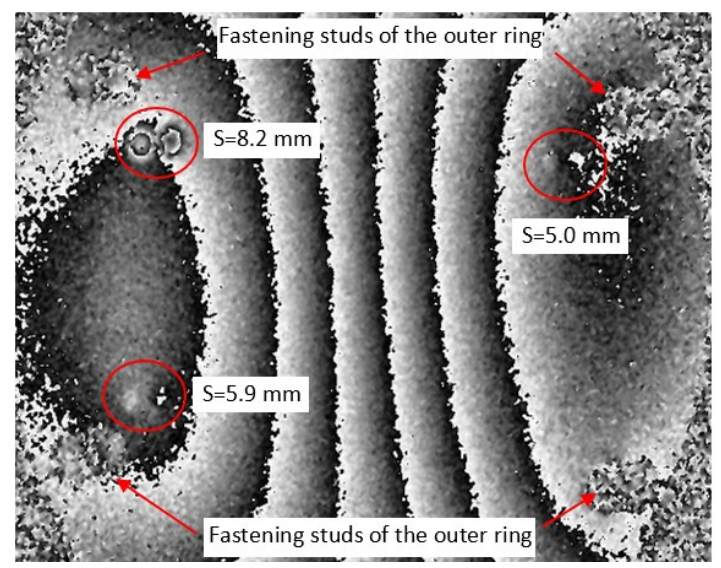


Fig. 14. Shearographic test results for the aluminum plate with five prefabricated defects whose thickness t = 0.5 mm, and three of which were founded at $\Delta p = 80$ kPa

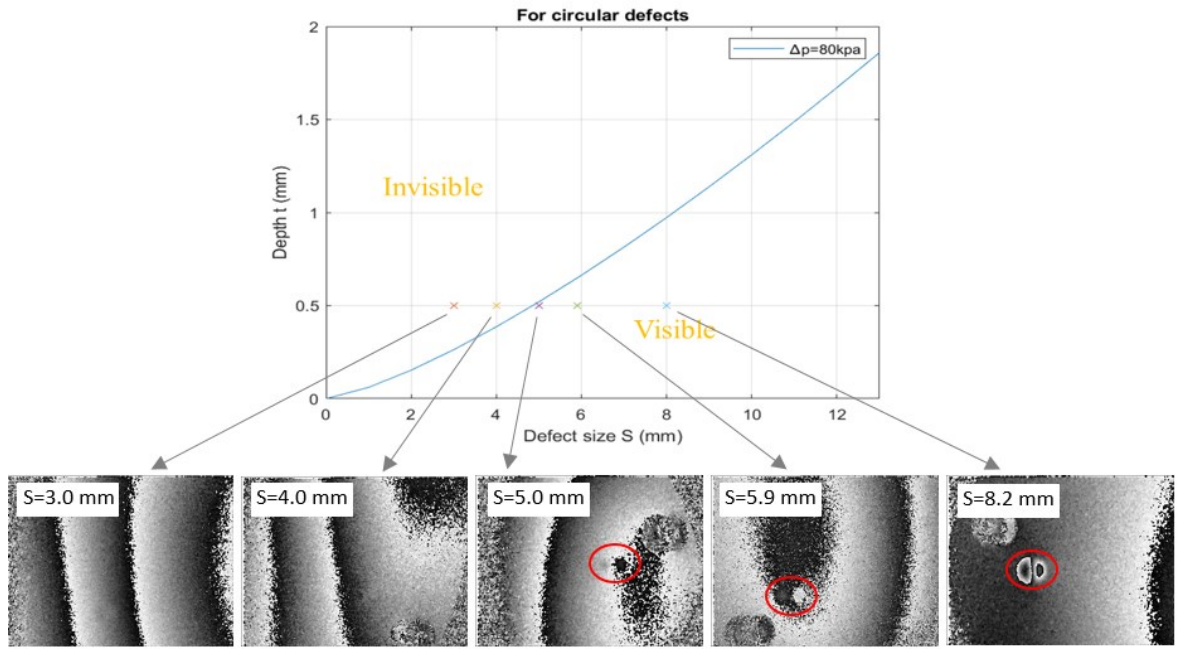


Fig. 15. A comparison between the simulated curve of the smallest detectable defect size and the shearograms measured in the area of each defect of the aluminum plate with five prefabricated defects with their depth t = 0.5 mm at $\Delta p = 80$ kPa.

To further validate the numerical curve, the other plate with five prefabricated defects of depth t = 0.5 mm and size ranging from S = 3, 4, 5, 5.9, and 8.2 mm, respectively, was tested by the digital shearographic setup. Fig. 15 shows the test result of the whole plate, three of the five defects, sizes 5.0, 5.9, and 8.2, were found at $\Delta p = 80$ kPa. A comparison between the numerical curve and the shearograms measured in the area of each defect with depth t = 0.5 mm is shown in Fig. 16. According to the numerical curve, only defects larger than 4.9 mm can be detected at the given

thickness and the load. The defects of size 3 mm and 4 mm can't be detected (see the left two shearograms), but defects with sizes of 5 mm, 5.9 mm, and 8.2 mm can be detected (see the right three shearograms). These experimental results again show very good agreement with the numerical curve at t = 0.5 mm and $\Delta p = 80$ kPa.

5. Analysis and Discussion

Experimental tests have been conducted to verify the numerical equations/curves developed in section 3. The experimental results have shown the reliability of the simulated equations/curves. In this section we will analyze the impact of various parameters on the test results and discuss application scopes and conditions of these numerical equations/curves.

There are five parameters in all of three developed models from Eqs. (14 - 16): the size of the smallest detectable defect S, the corresponding depth t, the loading magnitude Δp , the measuring sensitivity of the deformation in the middle of the defect w_{max} , and the term of material properties (E and ν). In this part, the impacts of these parameters on the size of the smallest detectable defect S will be analyzed. We still use the formula of the circular defects, i.e. Eq. (14), as an example for the analysis. Let's rewrite Eq. (14) as an expression of the size of the smallest detectable defect S, in term of thickness t, the load Δp , the measuring sensitivity of the deformation in the middle of defect Vmax, and the term of material properties (E and ν):

$$S(t, \Delta p, w_{max}) \Big|_{circular} = 4.4 \left[\frac{E}{(1-v^2)} \right]^{\frac{1}{4}} \left[w_{max} \right]^{\frac{1}{4}} \left[\frac{1}{\Delta p} \right]^{\frac{1}{4}} t^{\frac{3}{4}}$$
 (17)

Eq. (17) shows that the size of the smallest detectable defect S is proportional to $(w_{max})^{1/4}$, $[E/(1-v^2)]^{1/4}$, and $t^{3/4}$, and inversely proportional to the loading $\Delta p^{1/4}$. That means that a higher measuring sensitivity (i.e. smaller measurable w_{max}), less rigid materials (i.e. a smaller Young modulus), and a larger loading Δp can lead to finding a smaller S. However, the effect of each parameter on the S is not significant, because their impacts is only proportional to one-quarter power of these terms. An obvious influence on the S is the depth of the defect t which is proportional to S with three-quarters power. That means that a reduction of a defect depth will obviously enable the detection of a smaller defect, in other words, an increase in the depth of a defect will make it much more difficult to find.

Taking the circular defect as examples, i.e. Eq. (14), let's conduct a quantitative analysis below.

5.1. Impact of the measuring sensitivity of shearography:

Fig. 16 shows two curves depicting the relationships between the size of the smallest detectable defects S and the depth t at different test sensitivity of shearography " w_{max} " (w_{max} is smallest measurable deformation in the defect center). One is $w_{max} = 106$ nm and the other is $w_{max} = 53$ nm. Looking at the line of t = 1 mm, while the test sensitivity for w_{max} is increased from 106 nm to 53 nm, i.e. the test sensitivity is doubled, the size of the smallest detectable defect S is changed from

9.7 mm to 8.1 mm (about a 16% reduction). It is clear that the higher the test sensitivity, the smaller the defect size can be found, but its impact is not significant because S is only proportional to the $1/4^{th}$ power of w_{max} .

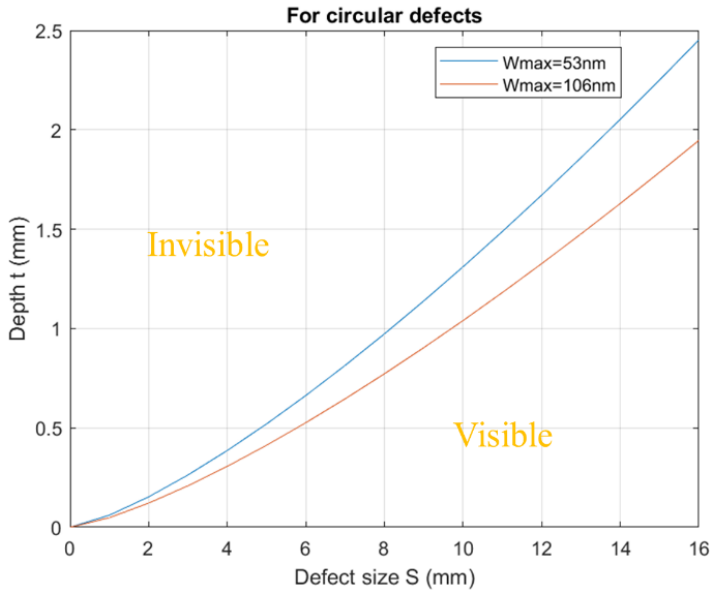


Fig. 16. Relationships between the size of the smallest detectable defect S and the depth t at different test sensitivity w_{max} (E = 70 Gpa, v = 0.33 and $\Delta p = 80$ kPa)

5.2. Impacts of the material properties and the load magnitude

The impacts of the material property term $[E/(l-v^2)]$ and the load magnitude Δp on the size of the smallest detectable defect S is similar to the measuring sensitivity presented in section 5.1 because S is only proportional to the $1/4^{th}$ power of material property's term and inversely proportional to the $1/4^{th}$ power of the loading magnitude. Therefore, the degree of influence on S is similar to the discussion in Section 5.1, i.e. if the Young modulus E decreases by half or the magnitude of loading Δp is doubled, the smallest detectable defect S will only be reduced by about 16%.

5.3. Impact of the depth of defect

The impact of the defect depth on the size of the smallest detectable defect can be found from Fig. 7. When the defect depth t is doubled, e.g. increases from 1 mm to 2 mm, looking at the curve of $\Delta p = 80$ kPa, the size of the smallest detectable defect S changes from 8.1 mm to 13.7 mm which is about a 69% change. This is because S is proportional to 3/4 power of t. Therefore, the depth of a defect t has a more obvious impact than the other three parameters. An increase of the depth of defects will lead to more difficulty in finding small defects.

5.4. Effect of defect shapes:

Regarding the effect of defect shapes, the square shape is the easiest shape to find small defects, the circular shape is similar to the square shape, and the rectangular shape with its small r value, i.e. very narrow defect, is the most difficult to detect. These phenomena can be observed from Figs. 7 - 9. It should be noted that the relationships between the size of the smallest detectable defect S and the depth t for an elliptical defect has not been presented due to its complexity, but because of its similarity to the rectangular equation, Eq. (15) can be approximately used to estimate ellipsoidal defects.

5.5. Applicability of the simulated models

The differential equation of the deformation presented in Eq. (5), and the analytical solutions (Eqs. (14-16)) are according to the plate theory. The upper part of a defect, i.e. the part from the top surface to the delamination or disbond, can be approximately regarded as a plate if the thickness t is much smaller than the defect size S [usually, $t < (1/5 \sim 1/8)S$]. Therefore, the analytical Eqs. (14-16) are suited for detecting near surface defects. Take t < S/6 as an example: if a defect size S = 12 mm, the equations and the curves developed are suited to detect defects whose depth is smaller than 2 mm, and if the defect size S = 36 mm, the equation and the curved are suited to detect defects whose depth t is smaller than 6 mm. This relationship gives a estimation between the defect size and the depth which it can be detected.

Regarding the materials suited for the models developed, the analytical Eqs. (14 to 16) are suited for any isotropic and quasi-isotropic materials as long as the Young's modulus and Poisson ratio can be considered independent of the directions. The composite materials for which the analytical solutions can be directly applied are:

 • Sheet Molding Compound (SMC) Carbon Fiber substrates, which have short fibers, randomly oriented.

• Short Fiber reinforced composites, which can have carbon or glass fiber reinforcements, and may have a thermoplastic matrix.

Sandwich structures with an isotropic face sheet (usually having a honeycomb-type core).

When dealing with woven fibers in regular patterns, some corrections may be necessary. For the purpose of the shearographic detection of delamination defects, the deformation calculated with the classical theories is adequate for quasi-isotropic composite substrates (such as $-60^{\circ}/0^{\circ}/60^{\circ}$ or $0/-45^{\circ}/45^{\circ}/90^{\circ}$). However, for more accurate results a correction factor to account for the shear stress between the plies can be used [46]. In these cases, the Young's modulus and Poisson ratio can be considered independent of the x and y coordinates.

This model is not easily applicable, instead, to unidirectional fiber composites, because of the lack of significant structural stiffness in the direction perpendicular to the fibers.

This model is also not suitable for detecting very deep defects without increasing the defect size. In this case, hybrid methods, such as shearography combined with the FEM method, have been reported [47-48]. They are effective under some specific conditions and occasions; however, in

general cases, shearography is not the best method to test very deep defects unless its size is large. This is because no surface information can be used for FEM or other numerical methods if the surface deformation caused by a load can't reach the measuring sensitivity of shearography, and this phenomenon is very possible if the defects are located very deep from surface. For detecting deep and small defects, methods like ultrasonic and x-ray techniques should be applied.

5.6. Boundary conditions and the loading methods

Regarding the determination of "visible" and "invisible" defects in the *S* - *t* curve, if a defect point falls right on the curve, theoretically, this defect size at the corresponding thickness is detectable under the given load magnitude. Any point in the area that is smaller than this size and larger than the thickness, i.e. points above the curve, will not be detectable. However, practically, the boundary conditions of actual defects are not 100% identical to the models. The boundary condition in the models developed is tightened all around representing the strictest boundary condition. If a defect can be found under this condition, then it will definitely be found in other boundary conditions. Thus, the visible areas, i.e. on and below the curve, are pretty accurate. However, points in the invisible region slightly above the curve could be visible depending on the actual boundary condition of defects, that means, a transition area exists slightly above the curve but it is difficult to indicate exactly in the figure due to the unknown boundary condition of the defects. Therefore, it is recommended that numerical models and curves be used to *estimate* the smallest detectable size and depth rather than use them for exact determination of the smallest detectable defect size.

Finally, it should be noted that the models developed correspond to a vacuum or a pressure loading. In a shearographic test, the best loading method is vacuum because it creates a pulling force as shown in Fig. 4b. A pulling force can separate delamination or disbond and cause a larger deformation and make the NDT of the defects easier. Although the vacuum loading is the best loading method, it is not the easiest loading method. The easiest loading method is by heating however the models presented in this paper is not suited for a heating loading. This is a future work and hopefully can be developed in the near future.

6. Conclusion

A numerical and experimental study of digital shearography for determining the size of the smallest detectable defect and the relationship with different parameters has been conducted. Numerical models to detect defects close to surface (usually, the defect depth *t* is smaller than 1/5 to 1/8 size of defect) and to determine the size of the smallest detectable defect by shearography under a vacuum and a pressure loading have been developed which provides first hand materials for test engineers before starting their investigations. The numerical models developed show that higher sensitivity for deformation measurement by shearography, less rigid material, larger loading magnitude, and shallower defects can lead to finding smaller defects. Of these four parameters, the most significant impact on defect inspection is the depth of the defect. An increase in the depth of the defect will obviously lead to more difficulty in finding the defect. The other three parameters: sensitivity for measuring deformation, material properties, and load magnitude, have the same weight for defect inspection and less impact than the defect depth *t*. This is because the size of the

- smallest detectable defect S is proportional to one-quarters power of each of the three parameters,
- but three-quarters the power of the defect depth t. The experimental validation of shearography
- demonstrated a very good agreement with the numerical models developed, which shows that the
- numerical models are a promising method to provide useful estimation for NDT by digital
- shearography. The models established in Eqs. (14-16) can be used to assist in the shearography
- inspection by estimating the size and depth of the smallest detectable defect with the corresponding
- load magnitudes.

CRediT authorship contribution statement

251

- Bicheng Guo: Methodology, Numerical Modelling, Experimental Validation, Writing partial
- original draft preparation. Xiaowan Zheng, Methodology, Numerical Modeling, Experimental
- Validation. Marco Gerini-Romagnoli: Conceptualization, Writing review & editing.
- 255 Lianxiang Yang: Conceptualization, Supervision, Writing partial original draft and revision
- preparation, Project administration.

257

Declaration of Competing Interest

258 259 260

The authors declare that they have no known competing financial interests or personal relationships that could have appeared to influence the work reported in this paper.

261262

Data Availability

263 264 265

Data will be made available on request.

266

267 Acknowledgements

268

- The research is partially supported by NSF IUCRC-Composite and Hybrid Materials Interfacing
- 270 (CHMI), USA. The authors would like to express their sincere thanks to Dr. Sayed Nassar, Dr.
- 271 Chuck Zhang, and Dr. Uday Vaidya, the directors of the centers of NSF IUCRC-CHMI of Oakland
- University, Georgie Tech, and the University of Tennessee, respectively, for their excellent
- leadership and support. Specials thanks also go to Drs. P. Balan, S. Shipp and Mr. Camillo
- 274 Archuleta from NSF for their support and guidance.

275

276 Reference

- 1. R. Zoughi, Microwave Non-Destructive Testing and Evaluation, Kluwer Academic Publishers, the Netherlands, 2000.
- L.J. Bond and M. Punjani, Review of some recent advances in quantitative ultrasonic NDT,
 IEE Proceedings A (Physical Science, Measurement and Instrumentation, Management and
 Education, Reviews), 1984, Volume 131, Issue 4, p. 265 –274, DOI: 10.1049/ip-a-
- 1.1984.0039.
- 3. S.I. Ganchev, R.J. Runser, N. Qaddoumi, E. Ranu, G. Carriveau, Microwave nondestructive evaluation of thick sandwich composites, Materials Evaluation, 1995 Volume 53, Issue 4, p. 463-467.

- 4. J.N. Butters, Application of ESPI to NDT, Optics & Laser Technology, 1977, Volume 9, Issue
 3, p. 117-12s.
- 5. Y. Y. Hung, Shearography: A New Optical Method for Strain Measurement and Nondestructive Testing, Optical Engineering, 1982, 21(3), 213391; https://doi.org/10.1117/12.7972920.
- 6. W. Steinchen, L. Yang, G. Kupfer, Digital shearography for nondestructive testing and vibration analysis, Experimental techniques, 1997, 21 (4), p. 20-23.
- 7. L. Yang, W. Steinchen, M. Schuth, and G. Kupfer, Precision measurement and nondestructive testing by means of digital phase shifting speckle pattern and speckle pattern shearing interferometry, Measurement, 1995, 16 (3), p. 149-160.
- 8. Clemente Ibarra-Castanedo, Stefano Sfarra, Dario Ambrosini, Domenica Paoletti, Abdelhakim Bendada, and Xavier Maldague, Diagnostics of panel paintings using holographic interferometry and pulsed thermography, Quantitative InfraRed Thermography Journal, 2010, Volume 7, Issue 1, p. 85-114.
- D. Balageas, X. Maldague, D. Burleigh, V. P. Vavilov, B. Oswald-Tranta, J. M. Roche, C.
 Pradere, G. M. Carlomagno, Thermal (IR) and Other NDT Techniques for Improved Material
 Inspection, J Nondestruct Eval (2016) 35:18, DOI 10.1007/s10921-015-0331-7.
- 10. L. Yang, W. Steinchen, M. Schuth, G. Kupfer, Noch präziser zerstörungsfrei Prüfen Anwendung der Phasenschiebetechnik in der elektronischen Shearografie, Technica 11, 1995,
 p. 19-22.
- 305 11. D. Francis, R.P. Tatam, and R.M. Groves, Shearography technology and applications: a review, 306 Measurement Science and Technology, 2010, Volume 21, Number 10, 102001.
- 12. Y. K. Zhu, G.Y. Tian, R.S. Lu, and H. Zhang, A Review of Optical NDT Technologies,
 Sensors, 2011, 11(8), 7773-7798; https://doi.org/10.3390/s110807773.
- 13. M.A. Abou-Khousa, A. Ryley, S. Kharkovsky, R. Zoughi1, D. Daniels, N. Kreitinger, and G.
 Steffes, Comparison of X Ray, Millimeter Wave, Shearography and Through Transmission
 Ultrasonic Methods for Inspection of Honeycomb Composites, AIP Conference Proceedings
 894, 999 (2007); https://doi.org/10.1063/1.2718076.
- 313 14. W Steinchen, L Yang, M Schuth, G Kupfer, Precision measurement and nondestructive testing 314 by means of the speckle and speckle-shearing interferometry, VDI Berichte 1118, 1994, 27
- 15. L. Yang, and Y.Y. Hung, Digital shearography for nondestructive evaluation and application in automotive and aerospace industries, Proceedings of the 16th WCNDT, Montreal, Canada,
 2004; http://www.ndt.net/article/wcndt2004/pdf/optical_techniques/534_yang.pdf.
- 16. Z.W. Liu, J. X. Gao, H. M. Xie, P. Wallace, NDT capability of digital shearography for different materials, Optics and Lasers in Engineering, Vol. 49 (12), 2011, P. 1462-1469.
- 17. W Steinchen, L. Yang, G Kupfer, P Mäckel, Non-destructive testing of aerospace composite materials using digital shearography, Proceedings of the Institute of Mechanical Engineers,
- Part G. Journal of Aerospace Engineering, Vol. 212 (1), 1998, p. 21-30, https://doi.org/10.1243/0954410981532108.
- 18. B. Zhang, X. Zheng, W. Xu, L. Yang, Overview of digital shearography for NDT, Materials Evaluation Vol. 78 (3), 2020, p. 343-351.

- 19. W. Steinchen and L.X. Yang, Digital Shearography: Theory and Application of Digital Speckle
 Pattern Shearing Interferometry, SPIE Press, 2003, Bellingham, WA, USA.
- 20. L. Yang and X. Xie, Digital Shearography: New developments and Applications, SPIE Press,
 2016, Bellingham, WA, USA.
- 21. L. Yang and T. Siebert, Chapter 22: Digital Speckle Interferometry in Engineering, p. 405-440,
 in the book entitled "New Directions of Holography and Speckles," edited by H. J. Caulfield
- and C. Vikram, American Scientific Publishers (ASP), 2008, ISBN: 1-58883-101-9.
- 22. D. Francis, Chapter 4: Non-destructive evaluation (NDE) of composites: introduction to
- shearography, in book "Non-Destructive Evaluation of Polymer Matrix Composites," edited
- by Vistasp M. Karbhari, Woodhead Publishing Series in Composites Science and Engineering,
- 336 2013, p. 56 83, ISBN 0-85709-344-4.
- 23. M. Y. Hung, L. Yang and Y.H. Huang, Chapter 5: Nondestructive evaluation (NDE) of composites: Digital Shearography, in book "Non-Destructive Evaluation of Polymer Matrix
- Composites," edited by Vistasp M. Karbhari, Woodhead Publishing Series in Composites
- Science and Engineering, 2013, p. 84-115, ISBN 0-85709-344-4.
- 341 24. John W. Newman, 7.13 Shearography Nondestructive Testing of Composites in book
- 342 "Reference Module in Materials Science and Materials Engineering: Comprehensive
- Composite Materials II," Elsevier, Volume 7, 2018, Pages 270-290,
- https://doi.org/10.1016/B978-0-12-803581-8.10046-3.
- 25. L. Yang and J. Li, Chapter 13: Shearography, in "Handbook of Advanced Non-Destructive
- Evaluation," edited by N. Ida, N. Meyendorf (eds.), Springer International Publishing AG,
- 347 2019, p. 383 420.
- 26. Y.Y. Hung, Shearography: A novel and practical approach for nondestructive inspection, Journal of Nondestructive Evaluation, Vol 8, 1989, p. 55–67.
- 27. F. Taillade, M. Quiertant, K. Benzarti, C. Aubagnac, Chapter 20: Non-destructive evaluation
- (NDE) of composites: using shearography to detect bond defect, in book "Non-Destructive
- Evaluation (NDE) of Polymer Matrix Composites," edited by Vistasp M. Karbhari, Woodhead
- Publishing Series in Composites Science and Engineering, 2013, p. 542-556, 557e, ISBN 0-
- 354 85709-344-4.
- 28. C. Petry, M. Schuth, Spatial phase shift shearography for enhanced NDT. NDT E. Int. 2018.
- 356 SHM-NDT 2018. Available online: https://www.ndt.net/article/shmndt2018/papers/SHM-
- 357 NDT-2018 paper 39. pdf (accessed on 4 January 2022).
- 358 29. L. Yang, F Chen, W Steinchen, MY Hung, Digital shearography for nondestructive testing:
- potentials, limitations, and applications, Journal of Holography and Speckle 2004, 1 (2), p. 69-
- 360 79.
- 361 30. E.C. Krutul, R.M. Groves, Opto-mechanical modelling and experimental approach to the
- measurement of aerospace materials using shearography and thermal loading. In: Bodermann
- B, editor. Model. Asp. Opt. Metrol. III, vol. 8083, SPIE; 2011, p. 434–442.
- 31. G. De Angelis, M. Meo, D.P. Almond, S.G. Pickering, S.L. Angioni, A new technique to detect
- defect size and depth in composite structures using digital shearography and unconstrained
- optimization. NDT&E Int 2012, 45(1), p. 91–96.

- 32. D. Akbari, N. Soltani, M. Farahani. Numerical and experimental investigation of defect detection in polymer materials by means of digital shearography with thermal loading. Proc Inst Mech Eng Part B J Eng Manuf, 2013, 227(3), p. 430–442.
- 33. X. Chen, M. Khaleghi, I. Dobrev, W. Tie, and C. Furlong, Structural Health Monitoring by Laser Shearography: Experimental and Numerical Investigations, Experimental and Applied Mechanics, Volume 6, 2015, pp 149–155, Proceedings of the 2014 Annual Conference on
- Experimental and Applied Mechanics.
- 34. F. Yang, X. Ye, Z. Qiu, B. Zhang, P. Zhong, Z. Liang, et al. The effect of loading methods and parameters on defect detection in digital shearography. Results Phys, 2017, 7, p. 3744-3755.
- 35. J.F. Vandenrijt, H. Xiong, C. Lequesne, P. Blain, Georges M. Shearography inspection of
 monolithic CFRP composites: finite element modeling approach for assessing an adequate
 strategy of artificial defects representing delamination. In: Lehmann P, Osten W, Jr. AAG,
 editors. Opt. Meas. Syst. Ind. Insp. XI, vol. 11056, SPIE; 2019, p. 107–13.
- 36. C. Vest, Holographic Interferometry, Wiley, New York, February 1979, ISBN: 0471906832.
- 37. W. Steinchen, L. Yang, M. Schuth, TV-shearography for measuring 3D-strains, Strain 32 (2), 1996, p. 49-58.
- 38. L. Zhu, Y. Wang, N. Xu, S. Wu, M. Dong, L. Yang, Real-time monitoring of phase maps of digital shearography. Optical Engineering. 2013, 52 (10), 101902.
- 385 39. X. Xie, X. Li, X. Chen, L. Yang, Review of recent developments of spatial phase-shift digital shearography, SPIE Vol. 9302 (2015), p. 49-60, Proceeding of the International Conference on Experimental Mechanics 2014,
- 40. Q. Zhao, X. Dan, F. Sun, Y. Wang, S. Wu, L. Yang, Digital shearography for NDT: phase measurement technique and recent developments, Applied Sciences 8 (12), 2662.
- 41. C. Petry, M. Schuth, Endoscopic spatial phase shift shearography with the Interferoskop for turbine blade flaw inspection, 11th International Symposium <NDT in Aerospace>, 13-15
 November 2019, Paris, https://www.ndt.net/article/aero2019/papers/fp we2a2 c petry.pdf.
- 42. M. Schuth and W. Buerakov, Handbuch Optische Messtechnik: Praktische Anwendungen für
 Entwicklung, Versuch, Fertigung und Qualitätssicherung, München, Hanser Verlag, 2017.
- 43. S. Timooshenko and W. S. Krieger, Theory of plates and Shells, McGraw-Hill Book Company,Inc., New York (1959).
- 44. Longfu Wang, Elastic Mechanics, Science Press of China, 137 Chaoyangmen Inner Street,
 Beijing (1979) (Chinese).
- 45. L. Yang, Grundlagen und Anwendungen der Phasenschiebe-Shearografie zur Zerstorungsfreien Werkstoffprufung, Dehnungsmessung und Schwingungsanalyse, PhD thesis, University of Kassel, Germany; Fortschritt-Berichte VDI, 1998, 8, 682.
- 46. C. W. Bert, A Critical Evaluation of New Plate Theories Applied to Laminated Composites, Composite Structures, 1984, Vol 2(4), pp. 329-347.
- 47. N. Tao, A. G. Anisimov, R. M. Groves, Shearography non-destructive testing of thick GFRP laminates: Numerical and experimental study on defect detection with thermal loading, Composite Structures, Volume 282, February 15th, 2022, 115008.

48. N. Tao, A. G. Anisimov, R. M. Groves, FEM-assisted shearography with spatially modulated heating for non-destructive testing of thick composites with deep defects, Composite Structures, Volume 297, October 1st, 2022, 115980.